Macromolecules

Cite This: Macromolecules 2018, 51, 6892−6900

Article

pubs.acs.org/Macromolecules

Quantification of Carbon Nanotube Liquid Crystal Morphology via Neutron Scattering

Francesca Mirri,[†,‡] Rana Ashkar,[∥,⊥,#] Vida Jamali,[†] Lucy Liberman,[%] Robert A. Pinnick,[†] Paul van der Schoot,[&,@] Yeshayahu Talmon,[%] Paul D. Butler,[∥] and Matteo Pasquali*[,†,‡,§]

[†]Department of Chemical and Biomolecular Engineering, [‡]Smalley-Curl Institute, and [§]Department of Chemistry, Rice University, Houston, Texas 77005, United States

[∥]NIST Center for Neutron Research, National Institute of Standard and Technology (NIST), Gaithersburg, Maryland 20899, United States

[⊥]Materials Science and Engineering Department, University of Maryland, College Park, Maryland 20742, United States

[#]Physics Department, Virginia Tech, Blacksburg, Virginia 24061, United States

[%]Department of Chemical Engineering and the Russell Berrie Nanotechnology Institute (RBNI), Technion-Israel Institute of Technology, Haifa 3200003, Israel

[&]Theory of Polymers and Soft Matter Group, Department of Applied Physics, Eindhoven University of Technology, 5600 MB Eindhoven, The Netherlands

[@]Institute for Theoretical Physics, Utrecht University, Princetonplein 5, 3584 CC Utrecht, The Netherlands

Supporting Information

ABSTRACT: Liquid phase assembly is among the most industrially attractive routes for scalable carbon nanotube (CNT) processing. Chlorosulfonic acid (CSA) is known to be an ideal solvent for CNTs, spontaneously dissolving them without compromising their properties. At typical processing concentrations, CNTs form liquid crystals in CSA; however, the morphology of these phases and their concentration dependence are only qualitatively understood. Here, we use small-angle neutron scattering (SANS), combined with polarized light microscopy and cryogenic transmission electron microscopy to study solution morphology over a range of concentrations and two different CNT lengths. Our results show that at the highest concentration studied the long CNTs form a highly ordered fully nematic phase, while short CNTs remain in a biphasic regime. Upon dilution, long CNTs undergo a 2D lattice expansion, whereas short CNTs seem to have an intermediate expansion between 2D and 3D probably due to the biphasic nature of the system. The average spacing between the CNTs scaled by the CNT diameter is the same in both systems, as expected for infinitely long aligned rods.

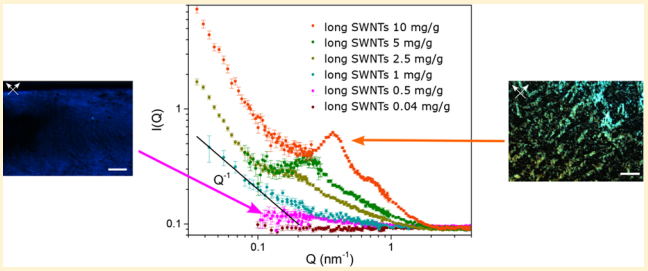

INTRODUCTION

Carbon nanotubes (CNTs) are characterized by outstanding electrical, mechanical, and thermal properties,[1−5] as well as low mass density, which make them an excellent candidate for many applications including photovoltaics, wearable electronics, biomedical connectors, aerospace structural materials, and thermal or electrical conductors.[3] To realize these applications, CNTs must be assembled into useful macrostructures. One of the most industrially attractive and promising routes for the fabrication of macroscopic CNT-based materials is liquid-state processing, mainly due to its scalability. However, dissolution via surface functionalization or suspension via additive dispersants and sonication can damage the intrinsic CNT characteristics (including their length), which in turn adversely affect the properties of ensuing macroscopic materials.[6]

Strong acids, in particular chlorosulfonic acid (CSA), are true solvents for CNTs.[7,8] CSA protonates the CNT walls, inducing short-range electrostatic repulsion forces that overcome the van der Waals attractions between CNTs.[9] Moreover, dissolution in CSA is reversible because CSA causes a CNT wall charge transfer rather than permanent electron removal; hence, no structural damage occurs to the CNTs.[9] Finally, CSA and other acids p-dope CNTs, which is advantageous in applications where electrical conductivity is needed. Although CSA and other CNT acid solvents were reported in 2004,[10] their potential usefulness in CNT processing has remained an open question. In 2009, Davis et al.[7] demonstrated that CSA is a practical processing solvent for

Received: May 13, 2018
Revised: August 9, 2018
Published: August 28, 2018

DOI: 10.1021/acs.macromol.8b01017
Macromolecules 2018, 51, 6892−6900

producing functional CNT materials and qualitatively showed, using cryogenic transmission electron microscopy (cryo-TEM), that CNTs individually dissolve in superacids. Subsequently, Parra-Vasquez et al.[8] showed that CSA can dissolve a broad range of CNTs irrespective of their length, as long as the CNTs have low defect density. Further developments enabled the processing of long CNTs via CSA dissolution for the continuous fabrication of CNT films,[11] coatings,[12] and fibers[13] with mechanical, electrical, and thermal properties that rival those of metals. CSA processing is now gaining wide adoption by many groups as a fabrication or postprocessing method.[14−18]

CNT−CSA solutions, similar to other rod-like particle suspensions, exhibit a transition from an isotropic solution (with randomly oriented rods) to a nematic liquid crystal solution (aligned rods yet no translational order) above a critical concentration that depends on the CNT aspect ratio.[7,19,20] In the absence of a macroscopic ordering field (such as shear), the liquid crystal phase consists of domains randomly oriented with respect to each other. As in other rod-like systems, such as tobacco mosaic virus,[21] and predicted theoretically by Onsager,[19] in a certain concentration range CNT−CSA solutions are biphasic, i.e., the isotropic and nematic phases coexist in equilibrium with each other[7,22] and can display various morphologies, from discrete tactoids to bicontinuous interspersed phases. Because of their finite diameter, lattice theories (which can only account for nearest-neighbor interactions) are expected to poorly describe the behavior of CNT solutions qualitatively; moreover, accounting for size polydispersity is imperative. For these reasons, Green et al.[23] extended Wensink and Vroege's treatment of polydisperse hard rods[24] (Onsager-like[19]) to account for long-range, solvent-mediated CNT−CNT interactions. This extended theory led to the prediction of the CNT−acid system phase boundaries, confirming that polydispersity broadens the biphasic region (as was already known from ref 24). It also predicted that the presence of residual, weak long-range attraction in weaker acids dramatically lowers the isotropic cloud point while having a relatively minor effect on the nematic cloud point—unless the acid becomes so weak as to lose the ability to separate CNTs and hence the LC phase is lost.

A thorough understanding of the phase behavior of CNT−CSA solutions is interesting per se, as CNTs can be synthesized and dissolved in ranges of aspect ratio and bending stiffness (persistence length) that are not accessible with other lyotropic nematogens. Moreover, work over the past decade shows that control over the solution phase is key to fabricating ordered CNT solids and hence to attaining desired properties.[13−15,25,26] Indeed, CNT alignment along the fiber axis is significantly improved when the CNTs are already aligned in solution before fiber spinning, and such alignment can be maintained with increasingly longer CNTs, resulting in enhanced mechanical strength and electrical conductivity of the spun fibers.[13,27]

From a characterization point of view, the study of CNT−CSA solutions has been challenging because of material compatibility issues (due to the acid corrosivity), sample preservation (the acids are extremely hygroscopic; the absorption of minimal water from the atmosphere can weaken the acid and compromise the phases), the inherently strong CNT absorption over a broad range of wavelengths of light (which limits the usefulness of optical microscopy), and the presence of hydrogen, sulfur, and chlorine in CSA (which leads to high neutron and X-ray scattering). Nonetheless, CNT−acid solutions have been studied by a variety of microscopy techniques, like cryo-TEM and cryogenic scanning electron microscopy (cryo-SEM), which allow tracking the phase transitions of the CNT−CSA system as a function of CNT concentration or aspect ratio.[20,28] However, despite the qualitative information obtained by microscopy techniques, a comprehensive quantitative assessment of the morphology of CNT phases under different conditions remains lacking.

Small-angle neutron scattering (SANS) is an ideal technique to quantitatively study bulk solution properties and has been successfully used to measure the dispersion quality of CNTs in aqueous media through the dependence of the scattering intensity on the momentum transfer, Q. Quantities such as network compactness and mesh size can be precisely determined from the scattering signal: for example, Wang et al.[29] and Fagan et al.[30] used SANS to study CNT agglomerate formation as a function of the surfactant concentration for a CNT−Triton X system and as a function of the pH for DNA-stabilized CNT dispersions, respectively; Yurekli et al.[31] studied the arrangement of surfactants on the CNT sidewalls; and Hough et al.[32] and Zhou et al.[33] determined the CNT mesh size from SANS for NaDDBS-stabilized CNT dispersions from the crossover between rigid rod and network behavior. SANS has also been effectively utilized in studying ordering and correlations in a myriad of liquid crystalline systems, including dispersions of CNTs with F-108 pluronic,[34] solutions of DNA,[35] tobacco mosaic virus,[36] and wormlike surfactant micelles.[37] For example, cellulose microfibrils in the nematic phase[38] show a peak in the scattering pattern that shifts to higher Q-values with increasing microfibril concentration. By tracking the peak position, the packing structure and the microfibril spacing in the nematic phase can be determined. Notably, a valiant effort was attempted in J. E. Fischer's group in the early 2000s to study the phase behavior of CNTs in deuterated fuming sulfuric acid via SANS, as reported in Zhou's doctoral thesis.[39] However, drawing any comparisons and conclusions from that study is difficult because the data resulted from a combination of embryonic sample preparation as well as incomplete qualitative understanding of the phase diagram.

Here, we use SANS, paired with polarized light microscopy (PLM) and cryo-TEM, to study CNTs (of two lengths) in CSA solutions at different concentrations ranging from isotropic to liquid crystalline phase. We find that CNT spacing within the solution changes depending on the CNT concentration, and we used this spacing to determine the type of expansion CNTs undergo upon dilution. In addition, the longest CNTs exhibit a second peak in the SANS signal at the highest concentration tested, showing that longer CNTs are characterized by a fully nematic phase.

MATERIALS AND EXPERIMENTAL SECTION

Two types of SWNT with two different aspect ratios were used: purified short SWNTs (HiPco 187.5 from Rice University, diameter = 0.94 ± 0.2 nm, length ≈ 0.42 μm, aspect ratio ≈ 440, density ≈ 1.7 g/cm^3) and purified long SWNTs (Meijo EC CNTs, purchased from Meijo Nano Carbon Co. Ltd., diameter = 2.02 ± 0.5 nm, length ≈ 8.8 μm, aspect ratio ≈ 4300, density ≈ 1.2 g/cm^3). Note that unless otherwise stated, uncertainties reported here represent ±1 standard deviation. Both CNT types were purified according to literature methods.[25,40] After purification, we assessed the CNT diameter by TEM (see the Supporting Information, section 1), obtained the aspect

DOI: 10.1021/acs.macromol.8b01017
Macromolecules 2018, 51, 6892−6900

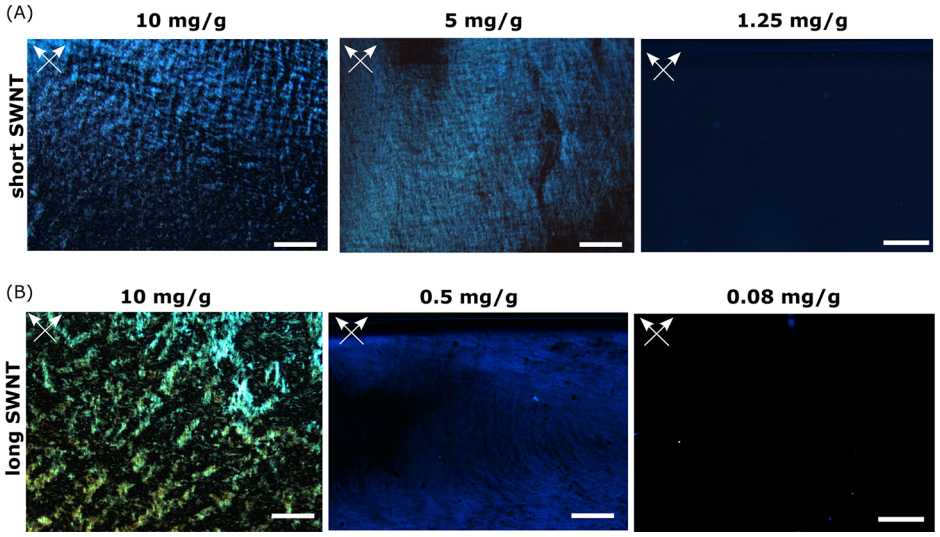

Figure 1. Polarized light micrographs for short (A) and long (B) SWNT solutions at different concentrations. The white arrows indicate the polarizer and analyzer directions, and the scale bar is 200 μm in all the images. The birefringence is indicative of the presence of a liquid crystalline phase that disappears at concentrations below 1.25 mg/g ($\Phi \approx 1.27 \times 10^{-3}$) for short SWNTs and 0.08 mg/g ($\Phi \approx 1.14 \times 10^{-4}$) for long SWNTs.

ratio by extensional rheology as described in ref 41, and calculated the CNT density based on the equation reported by Laurent et al.[42] (we use the equation for unfilled CNTs, although it is not clear whether CNTs are filled by CSA). On the basis of the measured diameter, we expect the CNT persistence length to range from 14 to 50 μm for the short CNT sample and from 118 to 536 μm for the long CNT sample.[43] The SWNTs were mixed with CSA (purchased from Sigma-Aldrich) at 10 mg/g and stirred overnight at room temperature. The solutions were then diluted with CSA (and stirred for about 1 h) to obtain the lower concentration regimes. Polarized light images of the solutions were taken using a Zeiss Axioplan microscope. For the high concentration samples, i.e., above 5 mg/g, a drop of solution was sandwiched between two glass slides and sealed. For lower concentration samples, i.e., below 2.5 mg/g, the solutions were imaged in flame-sealed glass capillaries.

Scattering measurements were performed at the NG7 30m SANS beamline at the Center for Neutron Research at the National Institute for Standards and Technology (NIST).[44] The solutions were loaded in Hellma quartz cells with a path length of 1 or 2 mm. The cells were sealed with Teflon caps followed by tight wrapping with Teflon tape to avoid moisture uptake. The scattering signal was normalized and corrected for all instrumental effects, such as empty cell scattering and background, using the NCNR Igor data reduction software.[45] The data fitting and analysis were done using the SasView software.[46]

For cryo-TEM measurements, we followed the methodology of Kleinerman et al.[28] A drop of CNT solution was applied to a perforated carbon film supported on a copper TEM grid (lacey Formvar/carbon films on 200 mesh Cu grids, from Ted Pella, Redding, CA), held by tweezers inside a controlled environment vitrification system (CEVS).[47] The entire CEVS was covered with a flexible polyethylene "glovebag" (Sigma-Aldrich). The CEVS was kept at 25 °C with continuous purging by pure dry nitrogen gas, preventing moisture penetration. To obtain good wettability of the support film, the perforated films were cleaned with glow discharge air-plasma (PELCO easiGlow, Ted Pella Inc., Redding, CA). A glass microfiber filter sheet was used for blotting the samples into thin films, followed by plunging into boiling liquid nitrogen (rather than freezing ethane to avoid interaction between CSA and organic material). The specimens were examined in a Philips CM120 TEM at an accelerating voltage of 120 kV. An Oxford CT3500 cryo-specimen holder was used to maintain the vitrified specimens below −175 °C in the TEM. The specimens were studied in the low-dose imaging mode to minimize electron beam radiation damage. Images were recorded digitally by a Gatan MultiScan 791 cooled-CCD camera.

RESULTS AND DISCUSSION

Solutions of each SWNT type were prepared at a concentration of 10 mg/g and were gradually diluted down to 0.04 mg/g. The measured concentrations were chosen such that they span values from the liquid crystalline phase down to the single isotropic phase. Figures 1A and 1B show the PLM micrographs for the short and long SWNT samples, respectively, at different concentrations. At high concentrations, the samples show birefringent areas, indicative of the presence of a liquid crystal phase; dark areas represent the isotropic phase or liquid crystalline regions where the CNTs are not at ±45° with respect to the crossed polarizers (indicated by the white arrows)—they can be distinguished by rotating the polarizers with respect to the sample. Below ≈1.25 mg/g (volume fraction $\Phi \approx 1.27 \times 10^{-3}$) for short SWNTs and ≈0.08 mg/g ($\Phi \approx 1.14 \times 10^{-4}$) for long SWNTs, birefringence disappears at all sample rotation angles; i.e., the solution is fully isotropic (isotropic cloud point). The ratio of the transition concentrations between the long and the short SWNTs (∼0.09) is approximately equal to the ratio between their inverse aspect ratios (∼0.1), as expected from Onsager's theory.[19]

Figure 2 reports SANS measurements at different solution concentrations for both short and long SWNTs. Scattering measurements were performed over the standard Q-range accessible by the SANS instrument, i.e., 0.03−4 nm^{-1} corresponding to length scales of ≈1.6 nm to ≈0.2 μm. The 2D SANS data (presented in Figure S2 of the Supporting Information) show isotropic signals due to the polydomain texture of the nematic phase, i.e., with domains containing highly aligned CNTs, while such domains are randomly oriented with respect to each other. Therefore, we cannot extract any information about the order parameter from our 2D SANS data based on the previous methods reported in the literature which rely on the anisotropic nature of the 2D scattering pattern.[48] The 2D data were hence circularly averaged to obtain the 1D plots of the scattering intensity, I, as a function of the momentum transfer, Q.

Figure 2 shows the scattering patterns obtained from the short and long SWNT solutions for concentrations from 0.04

DOI: 10.1021/acs.macromol.8b01017
Macromolecules 2018, 51, 6892−6900

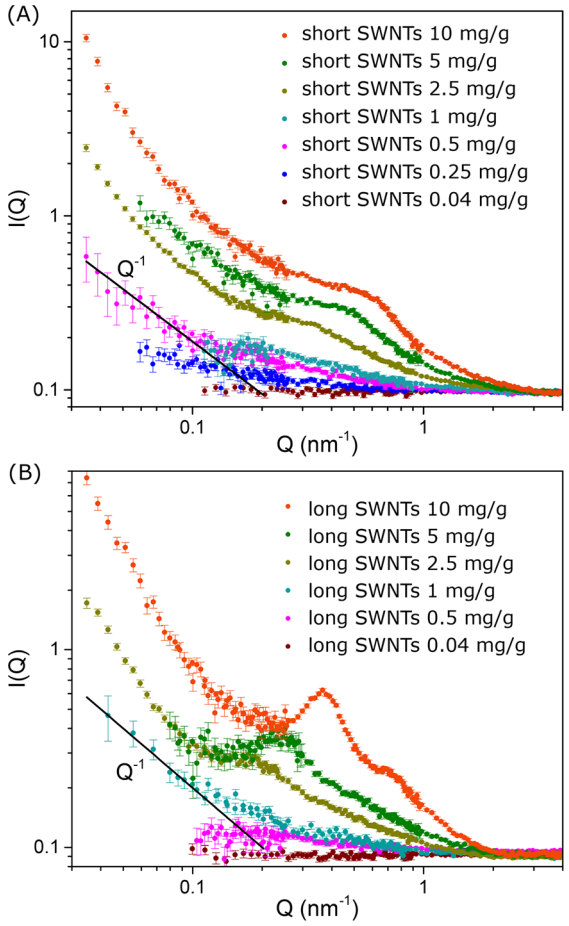

Figure 2. SANS data for short (A) and long (B) SWNT solutions. Both short and long SWNT solutions show a correlation peak at high concentrations, indicative of ordered SWNT structures in the samples, while at low concentrations the data patterns are suggestive of individualized SWNTs in solution. Error bars indicate ±1 standard deviation in all the plots. For the short SWNTs the concentrations reported in panel A correspond to the following volume fractions Φ: 1.02×10^{-2}, 5.09×10^{-3}, 2.54×10^{-3}, 1.02×10^{-3}, 5.09×10^{-4}, 2.54×10^{-4}, and 4.07×10^{-5}. For the long SWNTs the concentrations reported in panel B correspond to the following volume fractions Φ: 1.42×10^{-2}, 7.11×10^{-3}, 3.56×10^{-3}, 1.42×10^{-3}, 7.11×10^{-4}, and 5.69×10^{-5}.

to 10 mg/g. A broad correlation peak, indicative of positional ordering, is observed for concentrations above 2.5 mg/g ($\Phi \approx 2.54 \times 10^{-3}$) for the short SWNT solution and above 1 mg/g ($\Phi \approx 1.42 \times 10^{-3}$) for the long SWNT solution. This peak shifts to larger Q values with increasing concentration, suggesting increasingly tighter SWNT packing. Indeed, the position of this correlation peak is directly related to the nearest-neighbor spacing in the system. In a crystal structure, the characteristic length, d, is obtained from the peak position, Q^*, using Bragg's law: $d = 2\pi/Q^*$. Depending on the particular lattice formed in the system, d can then be related to the nearest-neighbor distance, e.g., $d \sin(60)$ for a hexagonal lattice.[38,49] In the absence of liquid structure factor models specifically developed for the system under study, the Bragg equation is often applied to liquid correlation peaks to obtain a rough estimate of the spacing by simply equating d with the nearest-neighbor spacing. In our case the actual peak position is obscured and altered by the rod form factor and, more importantly, by the strong underlying power law signal visible in the data. Thus, the peak positions were obtained from a more detailed structure factor analysis of the 1D SANS intensities (see section 2 in the Supporting Information). The average SWNT spacing is reported in Table 1 for the short and long SWNTs for the three highest concentrations at which the peak can be reliably observed (see the Supporting Information, section 2). Indeed, as the concentration decreases, the peaks broaden (see Figure 2) and become weaker in intensity down to a concentration of ≈1 mg/g, beyond which peaks are no longer resolvable by SANS.

The spacing normalized by the CNT diameter is nearly identical in the short and long CNT samples, as expected for high aspect ratio rods, because the volume fraction of these rods can be approximated as the ratio of the portions of the cross section of rods to the area of the lattice unit. The scattering patterns for the high concentration solutions show an upturn at low values of Q, most likely due to a transition into a Q^{-4} scattering regime coming from nematic domain boundary scattering and that would manifest at very low Q. However, at the lower concentration of 0.5 mg/g ($\Phi \approx 5.3 \times 10^{-4}$) the short SWNT system is well into the isotropic phase as shown by PLM. Thus, in this case, the low Q slope of ≈−1 (black line in Figure 2) in the scattering pattern, arising from the length scale of 60 nm, is consistent with individually dispersed rodlike nanoparticles.[50,51] On the other hand, at 1 mg/g ($\Phi \approx 1.42 \times 10^{-3}$) the PLM clearly shows that the long SWNT are still at least in a biphasic region despite the lack of resolvable peaks in the SANS data, as will be discussed later. Thus, the ≈−1 slope of the low Q scattering in this case (black line in Figure 2B) is most likely still affected by the tail of domain scattering despite the lack of resolvable peaks. Unfortunately, in the isotropic regime (below $\Phi \approx 1.15 \times 10^{-4}$), the concentration of long SWNTs is too small and the signal is too weak to capture the −1 Q slope of the scattered intensity.

Interestingly, long SWNT solutions show two correlation peaks at 10 mg/g ($\Phi \approx 1.42 \times 10^{-2}$) (corresponding to two concentric isotropic rings in the 2D pattern; section 3 in the Supporting Information). After applying the corrections described in section 2 of the Supporting Information, the position of these two major peaks are found to be at Q_1 = 0.365 nm^{-1} and Q_2 = 0. 737 nm^{-1}, giving a Q ratio of ≈1:2. The appearance of such a second-order peak at this Q ratio has been observed with increasing concentration in rodlike systems that form a nematic phase.[52−54] It only appears for the long SWNTs at the highest concentration because, at any given concentration, nematic ordering is stronger for longer rods.

Table 1. Real-Space Distance versus Solution Concentration for Short and Long SWNTs Obtained by SANS

concn (mg/g)	vol fractions Φ short SWNTs	vol fractions Φ long SWNTs	spacing (nm) short SWNTs	spacing (nm) long SWNTs	spacing normalized by short SWNT diam	spacing normalized by long SWNT diam
10	1.02×10^{-2}	1.42×10^{-2}	10.2 ± 0.1	17.2 ± 0.1	10.9 ± 2.31	8.6 ± 2.15
5	5.09×10^{-3}	7.11×10^{-3}	13.3 ± 0.2	25.5 ± 0.2	14.1 ± 3.02	12.7 ± 3.19
2.5	2.54×10^{-3}	3.56×10^{-3}	18.2 ± 0.2	34.5 ± 0.3	19.3 ± 4.12	17.3 ± 4.32

DOI: 10.1021/acs.macromol.8b01017
Macromolecules 2018, 51, 6892−6900

Although not stressed in the theoretical literature, this second peak is expected for sufficiently strongly aligned rodlike particles. Here, we calculated the structure factor $S(\mathbf{Q})$ as a function of the momentum transfer $\mathbf{Q}$ for a system of perfectly aligned, length-polydisperse rods interacting via a hard-core potential. $S(\mathbf{Q})$ is related to the scattering intensity $I(\mathbf{Q})$ and can be written as $S(\mathbf{Q}) = 1/(1 - n\langle\langle \hat{c}_{ij}(\mathbf{Q})\rangle\rangle)$. Here, n is the number density of solute, and $\langle\langle \hat{c}_{ij}(\mathbf{Q})\rangle\rangle$ is the average of the spatial Fourier transform of the direct correlation function $c_{ij}(\mathbf{r})$, describing short-range interactions between two rodlike particles of length L_i and L_j.[55] For our system, $c_{ij}(\mathbf{r})$ is assumed to be proportional to the Mayer function $f_{ij}(\mathbf{r})$ through $c_{ij}(\mathbf{r}) = \Gamma f_{ij}(\mathbf{r})$,[56] where $f_{ij}(\mathbf{r}) = \exp(-U_{ij}(\mathbf{r})/k_BT) - 1$ with $U_{ij}(\mathbf{r})$ the interaction potential, T the temperature, and k_B the Boltzmann constant. The factor Γ accounts for higher than two-body interactions in the thermodynamics of the fluid, even though the structure remains that of a second virial fluid. For hard particles, the Lee−Parsons theory applies: $\Gamma = (1 - 3\Phi/4)/(1 - \Phi)^2$, where Φ is the volume fraction of the rods in the solution.[55]

Strictly speaking, the SWNTs in solution interact via a hard-core repulsion, resulting from van der Waals interactions overcome by screened electrostatic interactions. We can model the SWNT−CSA system with a rescaled version of the hard-core repulsion, where the diameter of the rods, w, is increased to an effective diameter, w', due to the electrostatic charge on the rod walls. In this case, $U_{ij}(\mathbf{r}) = \infty$ if two particles overlap ($\mathbf{r} < w'$) and $U_{ij}(\mathbf{r}) = 0$ if they do not ($\mathbf{r} \geq w'$). The effective diameter, w', of the rods is defined as $w' = w + \alpha\kappa^{-1}$, where α is a free parameter and κ^{-1} is the Debye screening length; see the Supporting Information section 4 for details.

For a system with high length polydispersity (such as our long SWNTs with $p > 0.18$), we do not expect the formation of any positional ordering in the axial direction due to a direct transition from a nematic to a columnar phase (the smectic phase would be suppressed).[57,58] Therefore, the only features that arise in the structure factor are due to the short-range positional ordering in the perpendicular plane. Hence, for simplicity, we focus entirely on the perpendicular component of the $S(\mathbf{Q})$, i.e., $S(Q_\perp)$. Therefore, the structure factor expression reduces to

$$S(Q_\perp)^{-1} = 1 + 16\Phi'\Gamma \int_0^1 \mathrm{d}t\; tJ_0(Q_\perp w' t) \qquad (1)$$

where Φ' is the rescaled volume fraction given the effective diameter w' both in here and in calculating the factor Γ, and J_0 denotes a Bessel function of the first kind.

Figure 3 shows the structure factor $S(Q_\perp)$ at a volume fraction of 1.42×10^{-2} corresponding to 10 mg/g for our long SWNTs. The first two peaks are positioned at $Q_1 = 0.46$ nm^{-1} and $Q_2 = 1.03$ nm^{-1} with relative ratio of 1:2.2. This finding is in fair agreement with the $S(Q)$ obtained from the SANS data fitting (see Figure S1c of the Supporting Information) that revealed peaks at $Q_1 = 0.365$ nm^{-1} and $Q_2 = 0.737$ nm^{-1}. The discrepancy in the peak position might result from the error on the CNT diameter that affects the Debye length calculation as well as the density (hence volume fraction). Note that the peak ratio found with the theoretical model is 1:2.2 and not 1:2 as experimentally found. One reason is the assumption of perfect alignment of the rods—in reality, the CNTs are not perfectly aligned but have an angular spread which affects CNT packing. Additionally, the Lee−Parsons approximation that introduces the structure of a second virial fluid in our model for the interaction between the rods possibly affects the precise position of the peaks as well.

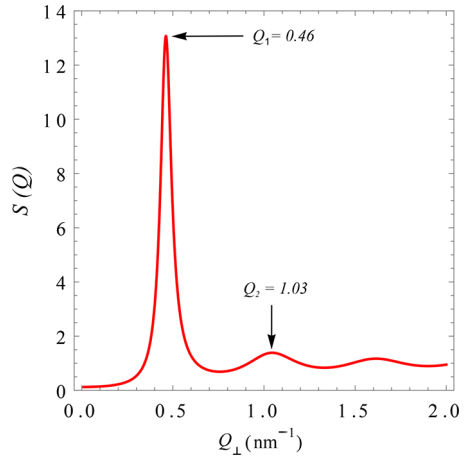

Figure 3. Structure factor $S(Q)$ versus the momentum transfer $Q_\perp$ in the cross-sectional plane. The relative spacing between peaks in the cross-sectional plane is 1:2.2, in fair agreement with the structure factor fitting to the SANS data.

To interpret the SANS data and gain better insight into the liquid crystalline nature of the CNT−CSA systems, we used an extension of the Onsager's theory[19] to estimate the transition concentration from biphasic to fully liquid crystalline regime, i.e., the nematic cloud point, and determine whether the systems are in a fully nematic or biphasic regimes. This model[23] is based on a square-well potential for a length polydisperse rigid-rod system. In brief, the potential is expressed as the sum of three contributions including the Onsager free energy, a term accounting for the effect of rod polydispersity following Wensink's model,[24] and an additional term that accounts for the effect of the short-range electrostatic repulsion and the long-range van der Waals attractions. The model inputs are solution concentration, isotropic cloud point concentration, length polydispersity σ (calculated as $\sigma = \sqrt{\frac{\langle L^2\rangle}{\langle L\rangle^2} - 1}$, where L is the CNT length), and CNT diameter (assumed to be monodisperse); the model provides an estimate of the nematic fraction, γ, of the system ($\gamma = 0$ at the isotropic cloud point and $\gamma = 1$ at the nematic cloud point). Our results suggest that at 10 mg/g ($\Phi \approx 1.1 \times 10^{-2}$) the short SWNT solution is characterized by the coexistence of a nematic liquid crystalline phase, ≈20 vol %, in equilibrium with an isotropic phase, ≈80 vol % (the nematic cloud point for the short SWNT system is at ≈22 mg/g; i.e., $\Phi \approx 2.3 \times 10^{-2}$). Conversely, for long SWNT solutions the system transitions to fully liquid crystalline regime above ≈1.9 mg/g ($\Phi \approx 2.8 \times 10^{-3}$). More information about the model parameters is reported in section 5 of the Supporting Information.

Cryo-TEM measurements were performed to confirm individualized SWNTs in the solution at low concentrations and verify the SWNT solution morphology at higher concentrations.[7,8,28,59] The highest solution concentration that enabled the preparation of sufficiently thin films for cryogenic-TEM imaging was 2.5 mg/g for both CNT types. Figure 4 shows cryo-TEM images for the short and long SWNT samples at concentrations from 0.04 to 2.5 mg/g. For short SWNTs, cryo-TEM images at 2.5 mg/g confirm the presence of an ordered liquid crystalline phase in equilibrium with the isotropic phase, corroborating PLM results (Figure 1)

DOI: 10.1021/acs.macromol.8b01017
Macromolecules 2018, 51, 6892−6900

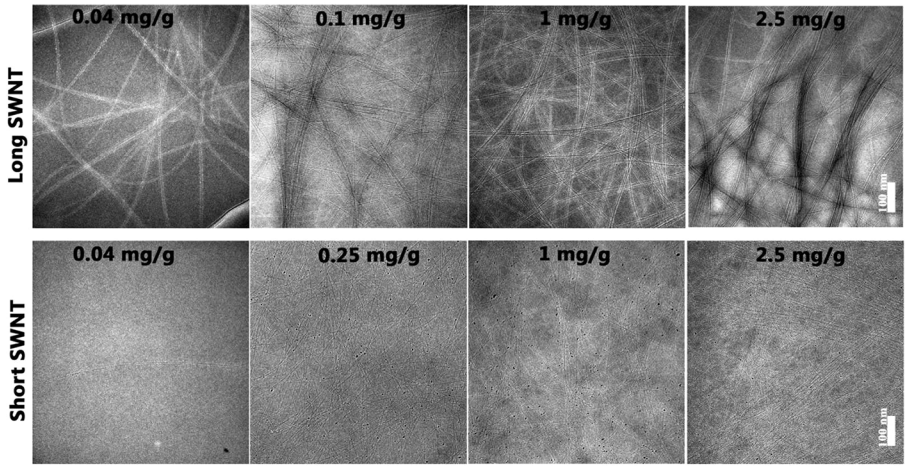

Figure 4. Cryo-TEM images for short and long SWNT solutions at different concentrations. The images show the presence of a liquid crystalline phase at 2.5 mg/g for short SWNTs. Sample preparation could be responsible for the bundled structures present at 1 and 2.5 mg/g for the long SWNTs. At 0.04 mg/g both short and long SWNTs are individually dissolved in the solvent. Black dots are the catalyst impurities in the sample.

and the theoretical predictions based on the extension of Onsager's theory. At 1 mg/g, the solution appears mostly isotropic with few narrow regions of aligned SWNTs. The apparent disagreement with our PLM data at the same concentration could be due to the PLM resolution not being sufficiently high to detect the presence of such narrow domains of liquid crystalline phase. At concentrations lower than 0.25 mg/g, the aligned regions of short SWNTs completely disappear, showing individualized SWNTs in an isotropic phase, in agreement with SANS and PLM results. Similar to the short SWNT system, long SWNT solutions also show individualized SWNTs in CSA at 0.04 mg/g, indicating full CNT dissolution in the dilute isotropic phase. The presence of ordered structures at high concentrations of long SWNTs is also evident in cryo-TEM micrographs for solutions with a SWNT content higher than 0.08 mg/g, as shown in Figure 4. However, sample preparation could also be responsible for the formation of the aligned bundled structures at 1 and 2.5 mg/g.

The transition from an ordered to a fully isotropic phase can be understood using the concentration dependence of the peak position of the liquid-ordered phase observed in the SANS data. Figure 5 shows the peak position, Q^*, as a function of SWNT concentration, Φ, for the long and short SWNT solutions at the three highest concentrations measured. As seen in Figure 5, both long and short SWNT systems show a concentration dependence of the correlation peak. We note that the liquid-order peak in SANS measurements is expected to shift with varying concentration for a sample in a fully liquid crystalline phase. However, no shift should be observed for a length monodisperse sample of rods in the biphasic regime because an increase in concentration would only change the relative fraction of isotropic and nematic phase within the solution and not the average distance between the rods. The systems presented in this work are characterized by high length polydispersity (σ = 0.434 and 0.397 for long SWNTs and for short SWNTs, respectively), which is known to cause a peak shift in the scattering signal[60] and to affect the relative concentration of rods in the isotropic and nematic phases in equilibrium with each other.[24] In a biphasic regime, when the concentration is increased, the longest rods form the nematic phase first, followed by increasingly shorter rods.[24] Using Wensink and Vroege' theoretical calculations reported in ref 24

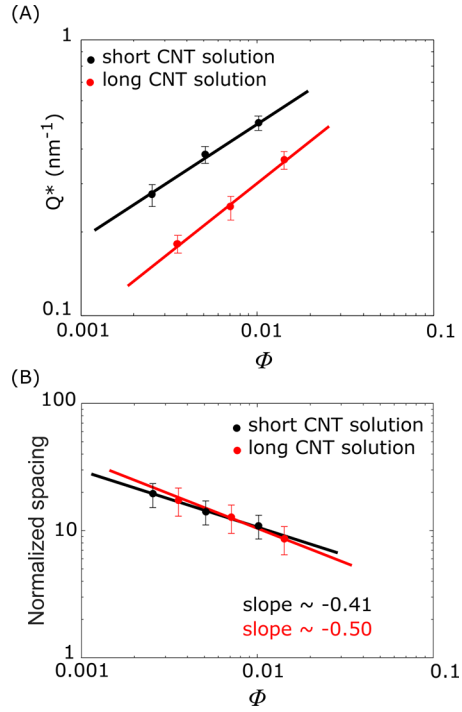

Figure 5. (A) Plot of the Q^* versus Φ showing different linear dependencies for the short and long SWNT solutions. The long SWNT system shows a slope of 0.5, whereas the short SWNT system shows a slope of 0.43. (B) Spacing normalized by CNT diameter (normalized spacing) versus volume fraction Φ showing different linear dependencies for the short and long SWNT solutions. The long SWNT system shows a slope of −0.5, whereas the short SWNT system shows a slope of −0.41.

and given the polydispersity of the parent solutions, the values of polydispersity for the nematic and isotropic shadow phases can be extracted. For our SWNT systems, we found that compared to the parent phase the nematic shadow phase for long SWNTs is 32% more polydisperse, while the isotropic shadow phase is 12% less polydisperse. On the other hand, for the short SWNT sample, the nematic shadow phase is 17% more polydisperse and the isotropic shadow phase is 10% less polydisperse than the parent phase. Consequently, the relative

DOI: 10.1021/acs.macromol.8b01017
Macromolecules 2018, 51, 6892−6900

polydispersity of coexisting nematic and isotropic daughter phases is expected to change when varying the parent concentration. This would affect the rod concentration in each phase and hence the rod-to-rod spacing in the daughter phases. Therefore, peak shifts in the SANS data are to be expected for both nematic and biphasic polydisperse systems, which is consistent with our scattering results on long and short SWNTs.

As shown in Figure 5, the main peak positions in the long SWNT scattering patterns exhibit a $\Phi^{1/2}$ behavior, whereas the short SWNT solutions follow a $Q^* \propto \Phi^{0.43}$ dependence. Typically, an exponent of 1/2 is indicative of a 2D expansion, which is expected for a fully nematic regime, characterized by orientational order but no positional order. Conversely, an exponent of 0.43 (intermediate value between 1/2 and 1/3) is indicative of an intermediate relaxation pattern between 2D and 3D, which is not surprising given the higher spatial freedom of the short SWNTs and the biphasic nature of the system at the concentrations tested. However, we note that within the error bars and the limited concentration range in Figure 5A the data could be consistent with $\Phi^{1/2}$ dependence if the presence of a biphasic phase was unknown. Moreover, the average spacing between the CNTs renormalized by their diameter is the same in both systems. This is expected for infinitely long rods (Figure 5B) because the volume fraction of rods can be approximated as the ratio of the cross section of rods to the area of the unit lattice. Because the SWNTs in this work have sufficiently high aspect ratio, the ordered phase can be thought of as an array of infinitely long packed nanorods, which can be treated entirely in 2D such that the area fraction (area of rods/area of solution) corresponds to the volume fraction Φ of the solution. Assuming a square lattice as typically done in the case of nematic systems,[38] one can relate the rod distance d, the rod cross section $\pi R_c^2/4$ (assuming an outer radius R_c), and the volume fraction (in lieu of area fraction) using the following expression: $d = \left(\frac{R_c^2}{\Phi}\right)^{1/2}$. If we use the approximation $d = 2\pi/Q^*$, we find that the main peak position depends on Φ and R_c as follows: $Q^* = \pi\left(\frac{4\Phi}{R_c^2}\right)^{1/2}$.

Fitting this equation to the values of Q^* from the SANS data and to the solution concentration converted to volume fraction Φ, we obtained a value of diameter ≈2.09 nm for the long SWNTs, which agrees with independently measured values of the diameter obtained from TEM (2.0 ± 0.5 nm). On the other hand, if we assume that the short SWNTs follow the same equation, i.e., assuming $\Phi^{1/2}$ dependence which is within the error margin in the data, we obtain a diameter ≈1.21 nm for the short SWNTs. This is in poor agreement with the TEM-extracted diameter of 0.94 ± 0.2 nm. This discrepancy is most likely due to the fact that the short SWNT system is in a biphasic regime and hence cannot be treated as fully nematic.

CONCLUSIONS

In summary, we exploited the contrast between CNTs and CSA in SANS to study the nanoscale morphology of bulk SWNT-CSA solutions along with complementary cryo-TEM and PLM measurements. Our results show that at low concentrations both short and long SWNTs are individually dispersed in solution, confirming that CSA is a true solvent for CNTs. At high concentrations, both SWNT types form a liquid crystalline phase, as evident from the PLM and SANS data. Our data indicate that upon dilution a 2D relaxation of the long SWNT packing in the plane normal to the SWNT length, whereas short SWNTs show an intermediate behavior between 2D and 3D expansion. Moreover, the average spacing between the CNTs renormalized by the CNT diameter is the same in both systems, as expected for infinitely long rods. In addition, at the highest concentration, long SWNTs exhibit a second-order peak in the SANS signal, indicating that these exceptionally high aspect ratio rods form a particularly well-ordered nematic phase with strong local positional order in the plane perpendicular to the CNT axis. This second peak has been theoretically predicted and is expected for rodlike nematic systems.

These results offer insight into the solution morphology of CNTs in CSA, which is particularly useful for CNT liquid processing; CNT fibers and films fabricated by liquid phase processing of CNT−CSA solutions highly benefit from CNT alignment in the liquid phase to improve the electrical conductivity and mechanical properties in the CNT alignment direction. An understanding of how CNTs arrange in a liquid phase for a given length and concentration brings significant advantage in determining the optimal range of processing conditions to maximize flow alignment and packing of the CNTs within the fiber structure. Additionally, aligning the domains in a polydomain nematic liquid crystal solutions such as CNT−CSA solution would further improve this overall alignment for achieving better macroscopic properties. This work opens up new possibilities for future research on flow alignment and packing of true CNT solutions. Such controlled studies would allow precise SWNT patterning and alignment in flow-processed coatings and films. This is a step toward a more thorough understanding of the morphology of CNTs in CSA for the optimization of liquid phase processing and fabrication of CNT multifunctional materials with optimal properties.

ASSOCIATED CONTENT

Supporting Information

The Supporting Information is available free of charge on the ACS Publications website at DOI: 10.1021/acs.macromol.8b01017.

TEM images of the CNTs, SANS fittings for short and long SWNT systems, SANS 2D plots for short and long CNT solutions, structure factor calculations, and parameters for the phase boundaries calculations for both CNT systems (PDF)

AUTHOR INFORMATION

Corresponding Author

*E-mail mp@rice.edu; Tel +1 713 348 5830 (M.P.).

ORCID

Rana Ashkar: 0000-0003-4075-2330
Yeshayahu Talmon: 0000-0002-9854-3972
Matteo Pasquali: 0000-0001-5951-395X

Author Contributions

F.M. and R.A. contributed equally to this work.

Notes

The authors declare no competing financial interest.

DOI: 10.1021/acs.macromol.8b01017
Macromolecules 2018, 51, 6892−6900

■ ACKNOWLEDGMENTS

We thank Dmitri E. Tsentalovich for providing the SWNT length. We thank Micah Green, Olga Kleinerman, and Yachin Cohen for useful discussions. Research was supported by Air Force Office of Scientific Research (AFOSR) Grants FA9550-12-1-0035 and FA9550-15-1-0370, Air Force Research Laboratories (AFRL) agreement FA8650-07-2-5061, the Robert A. Welch Foundation (C-1668), National Science Foundation (NSF) Grant CMMI-1025020, and United States−Israel Binational Science Foundation (BSF) Grants 2012223 and 2016161. Some of the measurements were conducted at the Center for Nanoscale Science and Technology, a user facility at NIST. This work benefited from the use of the SasView application, originally developed under NSF Award DMR-0520547 and currently maintained by NIST, UMD, ORNL, ISIS, ESS, and ILL. SasView also contains code developed with funding from the EU Horizon 2020 programme under the SINE2020 project Grant 654000. The cryo-TEM work was performed at the Technion Center for Electron Microscopy of Soft Materials, supported by the Technion Russell Berrie Nanotechnology Institute (RBNI). Identification of particular commercial products used in this work is intended for information purposes only and does not imply recommendation or endorsement by NIST.

■ REFERENCES

(1) Ruoff, R. S.; Lorents, D. C. Mechanical and thermal properties of carbon nanotubes. *Carbon* **1995**, *33*, 925−930.
(2) Treacy, M. M. J.; Ebbesen, T. W.; Gibson, J. M. Exceptionally high Young's modulus observed for individual carbon nanotubes. *Nature* **1996**, *381*, 678−680.
(3) Baughman, R. H.; Zakhidov, A. A.; de Heer, W. A. Carbon nanotubes - the route toward applications. *Science* **2002**, *297*, 787−792.
(4) Tans, S. J.; Devoret, M. H.; Dai, H. J.; Thess, A.; Smalley, R. E.; Geerligs, L. J.; Dekker, C. Individual single-wall carbon nanotubes as quantum wires. *Nature* **1997**, *386*, 474−477.
(5) Yakobson, B. I.; Avouris, P. Mechanical properties of carbon nanotubes. *Carbon Nanotubes* **2001**, *80*, 287−327.
(6) Lucas, A.; Zakri, C. c.; Maugey, M.; Pasquali, M.; van der Schoot, P.; Poulin, P. Kinetics of nanotube and microfiber scission under sonication. *J. Phys. Chem. C* **2009**, *113*, 20599−20605.
(7) Davis, V. A.; Parra-Vasquez, A. N. G.; Green, M. J.; Rai, P. K.; Behabtu, N.; Prieto, V.; Booker, R. D.; Schmidt, J.; Kesselman, E.; Zhou, W.; et al. True solutions of single-walled carbon nanotubes for assembly into macroscopic materials. *Nat. Nanotechnol.* **2009**, *4*, 830−834.
(8) Parra-Vasquez, A. N. G.; Behabtu, N.; Green, M. J.; Pint, C. L.; Young, C. C.; Schmidt, J.; Kesselman, E.; Goyal, A.; Ajayan, P. M.; Cohen, Y.; et al. Spontaneous dissolution of ultralong single- and multiwalled carbon nanotubes. *ACS Nano* **2010**, *4*, 3969−3978.
(9) Ramesh, S.; Ericson, L. M.; Davis, V. A.; Saini, R. K.; Kittrell, C.; Pasquali, M.; Billups, W. E.; Adams, W. W.; Hauge, R. H.; Smalley, R. E. Dissolution of pristine single walled carbon nanotubes in superacids by direct protonation. *J. Phys. Chem. B* **2004**, *108*, 8794−8798.
(10) Davis, V. A.; Ericson, L. M.; Parra-Vasquez, A. N. G.; Fan, H.; Wang, Y. H.; Prieto, V.; Longoria, J. A.; Ramesh, S.; Saini, R. K.; Kittrell, C.; et al. Phase Behavior and rheology of SWNTs in superacids. *Macromolecules* **2004**, *37*, 154−160.
(11) Mirri, F.; Ma, A. W. K.; Hsu, T. T.; Behabtu, N.; Eichmann, S. L.; Young, C. C.; Tsentalovich, D. E.; Pasquali, M. High-performance carbon nanotube transparent conductive films by scalable dip coating. *ACS Nano* **2012**, *6*, 9737−9744.
(12) Mirri, F.; Orloff, N.; Forster, A. M.; Ashkar, R.; Headrick, R. J.; Bengio, E. A.; Long, C.; Choi, A.; Luo, Y.; Hight Walker, A. R.; et al. Lightweight, flexible, high-performance carbon nanotube cables made by scalable flow coating. *ACS Appl. Mater. Interfaces* **2016**, *8*, 4903−4910.
(13) Behabtu, N.; Young, C. C.; Tsentalovich, D. E.; Kleinerman, O.; Wang, X.; Ma, A. W. K.; Bengio, E. A.; ter Waarbeek, R. F.; de Jong, J. J.; Hoogerwerf, R. E.; et al. Strong, light, multifunctional fibers of carbon nanotubes with ultrahigh conductivity. *Science* **2013**, *339*, 182−186.
(14) Bucossi, A. R.; Cress, C. D.; Schauerman, C. M.; Rossi, J. E.; Puchades, I.; Landi, B. J. Enhanced Electrical Conductivity in Extruded Single-Wall Carbon Nanotube Wires from Modified Coagulation Parameters and Mechanical Processing. *ACS Appl. Mater. Interfaces* **2015**, *7*, 27299−27305.
(15) Lu, Z.; Chao, Y.; Ge, Y.; Foroughi, J.; Zhao, Y.; Wang, C.; Long, H.; Wallace, G. G. High-performance hybrid carbon nanotube fibers for wearable energy storage. *Nanoscale* **2017**, *9*, 5063−5071.
(16) Zhang, Q.; Li, K.; Fan, Q.; Xia, X.; Zhang, N.; Xiao, Z.; Zhou, W.; Yang, F.; Wang, Y.; Liu, H.; Zhou, W. Performance improvement of continuous carbon nanotube fibers by acid treatment. *Chin. Phys. B* **2017**, *26*, 028802.
(17) Tran, T. Q.; Headrick, R. J.; Bengio, E. A.; Myo Myint, S.; Khoshnevis, H.; Jamali, V.; Duong, H. M.; Pasquali, M. Purification and Dissolution of Carbon Nanotube Fibers Spun from the Floating Catalyst Method. *ACS Appl. Mater. Interfaces* **2017**, *9*, 37112−37119.
(18) Wang, P.; Kim, M.; Peng, Z.; Sun, C.-F.; Mok, J.; Lieberman, A.; Wang, Y. Superacid-Surfactant Exchange: Enabling Nondestructive Dispersion of Full-Length Carbon Nanotubes in Water. *ACS Nano* **2017**, *11*, 9231−9238.
(19) Onsager, L. The effect of shape on the interaction of colloidal particles. *Ann. N. Y. Acad. Sci.* **1949**, *51*, 627−659.
(20) Kleinerman, O.; Liberman, L.; Behabtu, N.; Pasquali, M.; Cohen, Y.; Talmon, Y. Direct Imaging of Carbon Nanotubes Liquid Crystalline Phase Development in True Solutions. *Langmuir* **2017**, *33*, 4011−4018.
(21) Bernal, J. D.; Fankuchen, I. X-Ray and Crystallographic studies of plant virus preparations: I. Introduction and preparation of specimens II. Modes of aggregation of the virus particles. *J. Gen. Physiol.* **1941**, *25*, 111−146.
(22) Jamali, V.; Behabtu, N.; Senyuk, B.; Lee, J. A.; Smalyukh, I. I.; van der Schoot, P.; Pasquali, M. Experimental realization of crossover in shape and director field of nematic tactoids. *Phys. Rev. E* **2015**, *91*, 042507.
(23) Green, M. J.; Parra-Vasquez, A. N.; Behabtu, N.; Pasquali, M. Modeling the phase behavior of polydisperse rigid rods with attractive interactions with applications to single-walled carbon nanotubes in superacids. *J. Chem. Phys.* **2009**, *131*, 084901.
(24) Wensink, H. H.; Vroege, G. J. Isotropic-nematic phase behavior of length-polydisperse hard rods. *J. Chem. Phys.* **2003**, *119*, 6868−6882.
(25) Tsentalovich, D. E.; Headrick, R. J.; Mirri, F.; Hao, J.; Behabtu, N.; Young, C. C.; Pasquali, M. Influence of Carbon Nanotube Characteristics on Macroscopic Fiber Properties. *ACS Appl. Mater. Interfaces* **2017**, *9*, 36189−36198.
(26) Yang, C.; Trikantzopoulos, E.; Jacobs, C. B.; Venton, B. J. Evaluation of carbon nanotube fiber microelectrodes for neurotransmitter detection: Correlation of electrochemical performance and surface properties. *Anal. Chim. Acta* **2017**, *965*, 1−8.
(27) Headrick, R. J.; Tsentalovich, D. E.; Berdegué, J.; Bengio, E. A.; Liberman, L.; Kleinerman, O.; Lucas, M. S.; Talmon, Y.; Pasquali, M. Structure−property relations in carbon nanotube fibers by downscaling solution processing. *Adv. Mater.* **2018**, *30*, 1704482.
(28) Kleinerman, O.; Parra-Vasquez, A. N. G.; Green, M.; Behabtu, N.; Schmidt, J.; Kesselman, E.; Young, C.; Cohen, Y.; Pasquali, M.; Talmon, Y. Cryogenic-temperature electron microscopy direct imaging of carbon nanotubes and graphene solutions in superacids. *J. Microsc.* **2015**, *259*, 16−25.
(29) Wang, H.; Zhou, W.; Ho, D. L.; Winey, K. I.; Fischer, J. E.; Glinka, C. J.; Hobbie, E. K. Dispersing single-walled carbon

DOI: 10.1021/acs.macromol.8b01017
Macromolecules 2018, 51, 6892−6900

nanotubes with surfactants: a small angle neutron scattering study. *Nano Lett.* **2004**, *4*, 1789−1793.
(30) Fagan, J.; Landi, B.; Mandelbaum, I.; Simpson, J.; Bajpai, V.; Bauer, B.; Migler, K.; Hight Walker, A.; Raffaelle, R.; Hobbie, E. Comparative measures of single-wall carbon nanotube dispersion. *J. Phys. Chem. B* **2006**, *110*, 23801−23805.
(31) Yurekli, K.; Mitchell, C. A.; Krishnamoorti, R. Small-Angle Neutron Scattering from Surfactant-Assisted Aqueous Dispersions of Carbon Nanotubes. *J. Am. Chem. Soc.* **2004**, *126*, 9902−9903.
(32) Hough, L.; Islam, M.; Hammouda, B.; Yodh, A.; Heiney, P. Structure of semidilute single-wall carbon nanotube suspensions and gels. *Nano Lett.* **2006**, *6*, 313−317.
(33) Zhou, W.; Islam, M.; Wang, H.; Ho, D.; Yodh, A.; Winey, K. I.; Fischer, J. E. Small angle neutron scattering from single-wall carbon nanotube suspensions: evidence for isolated rigid rods and rod networks. *Chem. Phys. Lett.* **2004**, *384*, 185−189.
(34) Jang, H.-S.; Do, C.; Kim, T.-H.; Choi, S.-M. Single-Walled Carbon Nanotube-Induced Lyotropic Phase Behavior of a Polymeric System. *Macromolecules* **2012**, *45*, 986−992.
(35) Borsali, R.; Nguyen, H.; Pecora, R. Small-angle neutron scattering and dynamic light scattering from a polyelectrolyte solution: DNA. *Macromolecules* **1998**, *31*, 1548−1555.
(36) Maier, E. E.; Krause, R.; Deggelmann, M.; Hagenbuechle, M.; Weber, R.; Fraden, S. Liquidlike order of charged rodlike particle solutions. *Macromolecules* **1992**, *25*, 1125−1133.
(37) Chen, S.; Sheu, E. Y.; Kalus, J.; Hoffman, H. Small-angle neutron scattering investigation of correlations in charged macromolecular and supramolecular solutions. *J. Appl. Crystallogr.* **1988**, *21*, 751−769.
(38) Orts, W.; Godbout, L.; Marchessault, R.; Revol, J.-F. Enhanced ordering of liquid crystalline suspensions of cellulose microfibrils: A small angle neutron scattering study. *Macromolecules* **1998**, *31*, 5717−5725.
(39) Zhou, W. Structural characterization of macroscopic single-walled carbon nanotube materials. PhD Thesis, University of Pennsylvania, 2005.
(40) Xu, Y.; Peng, H.; Hauge, R. H.; Smalley, R. E. Controlled Multistep Purification of Single-Walled Carbon Nanotubes. *Nano Lett.* **2005**, *5*, 163−168.
(41) Tsentalovich, D. E.; Ma, A. W.; Lee, J. A.; Behabtu, N.; Bengio, E. A.; Choi, A.; Hao, J.; Luo, Y.; Headrick, R. J.; Green, M. J.; Talmon, Y.; Pasquali, M. Relationship of Extensional Viscosity and Liquid Crystalline Transition to Length Distribution in Carbon Nanotube Solutions. *Macromolecules* **2016**, *49*, 681−689.
(42) Laurent, C.; Flahaut, E.; Peigney, A. The weight and density of carbon nanotubes versus the number of walls and diameter. *Carbon* **2010**, *48*, 2994−2996.
(43) Fakhri, N.; Tsyboulski, D. A.; Cognet, L.; Weisman, R. B.; Pasquali, M. Diameter-dependent bending dynamics of single-walled carbon nanotubes in liquids. *Proc. Natl. Acad. Sci. U. S. A.* **2009**, *106*, 14219−14223.
(44) Glinka, C.; Barker, J.; Hammouda, B.; Krueger, S.; Moyer, J.; Orts, W. The 30 m small-angle neutron scattering instruments at the National Institute of Standards and Technology. *J. Appl. Crystallogr.* **1998**, *31*, 430−445.
(45) Kline, S. R. Reduction and analysis of SANS and USANS data using IGOR Pro. *J. Appl. Crystallogr.* **2006**, *39*, 895−900.
(46) Doucet, M.; et al. SasView version 4.1, Zenodo, 4.0.1; http://doi.org/10.5281/zenodo.438138 (accessed 2015).
(47) Bellare, J. R.; Davis, H.; Scriven, L.; Talmon, Y. Controlled environment vitrification system: an improved sample preparation technique. *J. Electron Microsc. Technol.* **1988**, *10*, 87−111.
(48) Davidson, P.; Petermann, D.; Levelut, A. M. The Measurement of the Nematic Order Parameter by X-ray Scattering Reconsidered. *J. Phys. II* **1995**, *5*, 113−131.
(49) Butler, P. D.; Hamilton, W. A.; Magid, L. J.; Hayter, J. B.; Slawecki, T. M.; Hammouda, B. Use of complementary neutron scattering techniques in studying the effect of a solid/liquid interface on bulk solution structures. *Faraday Discuss.* **1996**, *104*, 65−78.
(50) Kim, T. H.; Doe, C.; Kline, S. R.; Choi, S. M. Water-Redispersible Isolated Single-Walled Carbon Nanotubes Fabricated by In Situ Polymerization of Micelles. *Adv. Mater.* **2007**, *19*, 929−933.
(51) Kim, T.-H.; Doe, C.; Kline, S. R.; Choi, S.-M. Organic solvent-redispersible isolated single wall carbon nanotubes coated by in-situ polymerized surfactant monolayer. *Macromolecules* **2008**, *41*, 3261−3266.
(52) Petukhov, A. V.; Meijer, J.-M.; Vroege, G. J. Particle shape effects in colloidal crystals and colloidal liquid crystals: Small-angle X-ray scattering studies with microradian resolution. *Curr. Opin. Colloid Interface Sci.* **2015**, *20*, 272−281.
(53) Paineau, E.; Krapf, M.-E. M.; Amara, M.-S.; Matskova, N. V.; Dozov, I.; Rouziere, S.; Thill, A.; Launois, P.; Davidson, P. A liquid-crystalline hexagonal columnar phase in highly-dilute suspensions of imogolite nanotubes. *Nat. Commun.* **2016**, *7*, 10271.
(54) Grelet, E.; Rana, R. From soft to hard rod behavior in liquid crystalline suspensions of sterically stabilized colloidal filamentous particles. *Soft Matter* **2016**, *12*, 4621−4627.
(55) Hansen, J.-P.; McDonald, I. R. *Theory of Simple Liquids: With Applications to Soft Matter*; Academic Press: 2013.
(56) van der Schoot, P. The nematic-smectic transition in suspensions of slightly flexible hard rods. *J. Phys. II* **1996**, *6*, 1557−1569.
(57) Bates, M. A.; Frenkel, D. Influence of polydispersity on the phase behavior of colloidal liquid crystals: A Monte Carlo simulation study. *J. Chem. Phys.* **1998**, *109*, 6193−6199.
(58) Bohle, A. M.; Hołyst, R.; Vilgis, T. Polydispersity and ordered phases in solutions of rodlike macromolecules. *Phys. Rev. Lett.* **1996**, *76*, 1396.
(59) Behabtu, N.; Lomeda, J. R.; Green, M. J.; Higginbotham, A. L.; Sinitskii, A.; Kosynkin, D. V.; Tsentalovich, D.; Parra-Vasquez, A. N.; Schmidt, J.; Kesselman, E.; et al. Spontaneous high-concentration dispersions and liquid crystals of graphene. *Nat. Nanotechnol.* **2010**, *5*, 406−411.
(60) van der Kooij, F. M.; Kassapidou, K.; Lekkerkerker, H. N. Liquid crystal phase transitions in suspensions of polydisperse plate-like particles. *Nature* **2000**, *406*, 868−871.

DOI: 10.1021/acs.macromol.8b01017
Macromolecules 2018, 51, 6892−6900